




Optical characterizations of lightly doped $(\text{PbS})_{1-x}\text{Zn}_x$ thin films influenced by film thickness and annealing temperature for applications in highly intensive radiation systems

E. Kh. Shokr¹, W. S. Mohamed^{1,2}, A. G. Adam^{1,*} , and H. M. Ali¹

¹ Physics Department, Faculty of Science, Sohag University, Sohag 82524, Egypt

² Physics Department, College of Science, Jouf University, Al-Jouf, P.O. Box 2014, Sakaka, Saudi Arabia

Received: 12 June 2023

Accepted: 6 September 2023

Published online:

3 October 2023

© The Author(s), 2023

ABSTRACT

The lightly Zn-doped $(\text{PbS})_{1-x}(\text{Zn})_x$ thin films were synthesized by the thermal deposition technique. The structure, morphology, and elemental analyses were carried out by XRD, SEM, and EDS, respectively, and characterised by UV–VIS–NIR spectroscopy. The optical absorption, transmission, and reflection have been studied and analysed. The linear and non-linear parameters have been determined, explained, and compared with the reported results. The effects of Zn-doping, film thickness, and annealing temperature on NLO-parameters have been considered. The better 2.78×10^{-10} and 2.93×10^{-10} esu values of the non-linear refractive index n_2 and 3rd-order optical polarizability $\chi^{(3)}$, respectively, were attained by $(\text{PbS})_{0.97}(\text{Zn})_{0.03}$ film of 150 nm thick annealed at 200 °C.

1 Introduction

Chalcogenide glassy materials are advantageous over crystalline ones because of their smooth tuning property, low cost, and significant efficiency in optoelectronic applications [1–6]. Lead sulfide (PbS) is an important narrow direct band gap semiconductor with several excellent physical and chemical properties [7, 8]. It has numerous applications, such as tunable near-infrared detectors [9, 10], biological markers [11, 12], thermoelectric materials [13], photocatalysts [14], quantum dot solar cells [15], and new-generation solar cells [16–19]. PbS belongs to the IV–VI group of semiconductor compounds with face-centered cubic

(fcc) crystal structures [20]. In addition, PbS is a P-type semiconductor with high light absorbing capacity in the visible and NIR ranges due to its tunable band gap within this spectral range [21–23], recommending it as an excellent P-type absorber for solar cells [24].

The films of PbS have been grown in many forms for current applications using a variety of techniques, including chemical bath deposition (CBD), vacuum evaporation, spray pyrolysis, electrochemical deposition, etc. [25–28].

The study and characterization of linear optical absorption, dielectric, and dispersion, in addition to the calculation of related parameters like the extinction coefficient, refractive index, and energy gap, are crucial for the optical

Address correspondence to E-mail: ahmedgamaladam11@gmail.com

material properties and performance of optoelectronic devices.

When a material is exposed to a strong light beam, the polarisation becomes non-linear proportional to the electric field, and non-linear effects appear to dominate. This suggests that linear and non-linear susceptibilities can participate in the susceptibility contribution to polarizability (P).

The non-linear refractive index $n^{(2)}$ and the third order of non-linear susceptibility $\chi^{(3)}$ are important parameters utilised to achieve optically limiting behaviour and are used in a variety of applications. Values of n_2 and $\chi^{(3)}$ are strongly enhanced by different factors, such as the polarizable bond density and their orientations with respect to the induced electric field, the material compactness, the bond length of polarizable species, the density of localised states, the density of cloud electrons in the outer shell and their distance from the nucleus, etc. [29]. It is believed that PbS could be promising as non-linear optical (NLO) candidates because of their large refractive nonlinearity and high 3rd-order non-linear optical susceptibility [30]. That is because of the great density of electrons in Pb⁸² placed far apart from the nucleus, large Pb–S bond length of 0.29696 nm [31, 32] in addition to the easy formation of polarizable atoms and ions in chalcogenide glasses induced by high electric fields.

The dopant nature and concentration can play important roles in tuning the physical properties and efficiencies of Pbs-based devices. The incorporation of zinc atoms as a doping element into the PbS crystal structure leads to defect formation, increasing the density of polarizable species that can respond to intensive fields [31, 33]. Zn²⁺ with a radius of 0.74 Å occupies the sites of Pb²⁺ with a radius of 1.19 Å [34] as a substitutional element and results in a shrinkage of the lattice [35], a matter that leads to a material compactness increase and, in turn, a refractive index increase.

In this work, the optical linear and non-linear properties of (PbS)_{1-x}(Zn)_x thin films prepared by thermal deposition have been investigated. The effects of Zn-doping, film thickness, and annealing temperature have been examined. The results were discussed and compared with the corresponding reported ones..

2 Experimental

Both un-doped and Zn-doped PbS thin films with different thicknesses from 50 to 250 nm were deposited on glass substrates using the thermal

evaporation method by the Edwards E306A coating system. During the preparation of our films, the deposition rate changed from 1.2 to 3.5 Å/s. The chamber was evacuated to 4×10^{-4} mbar at the start of the deposition process and 3.63×10^{-5} mbar at the end. High purity of 99.99% PbS and Zn powders provided by the Aldrich Association were used for the present samples. The powder mixture of (PbS)_{1-x}(Zn)_x ($x = 0, 0.01, 0.03, 0.05$ wt%) was prepared from the high purity stoichiometric amounts of (Zn and PbS). Then, the mixture was cold pressed in tablet form. In order to obtain homogeneous compounds, the mixtures of samples are heated for 2 h at 300 °C, 3 h at 350 °C and 2 h at 400 °C. The samples were milled again for 2 h and the resultant powders were pressed into tablets. These tablets have been sintered at 600 °C for 3 h to ensure the homogeneity of the forming compounds, that were used as sources of our thin films. These tablets were placed in a molybdenum boat (melting point around ≈ 2620 °C).

The compressed tablets of un-doped and Zn-doped PbS were deposited on clean glass substrates, washed by acetone, and cleaned in heated distilled water using an ultrasonic cleaner (VGT-1613 QTD) with a digital timer of 2000 mL capacity. A digital film thickness monitor, model INFICON, was used to measure the film thickness and the rate of deposition (SQM-160).

The crystallographic structure of the as-deposited films on glass was investigated by X-ray diffraction pattern (Bruker D8 Advance—Germany) with Cu as a target and Ni as a filter (Cu α_1 ; $\lambda = 1.5406$ Å) at 30 kV and 30 mA with scanning speed equal to 2.5°/min.

The surface morphology and compositional contents of the present (PbS)_{1-x}Zn_x films were examined using field emission scanning electron microscopy (FE-SEM) JSM-6100 (JEOL, Japan) microscope with a 30 kV acceleration voltage. Using the FE-energy SEM's dispersive analysis of X-ray (EDAX) instrument, the chemical compositions of the films were also examined using (EDS unit, HNU5000, USA). A very thin film of gold, about 10 nm thick, was applied to the samples prior to the examination.

The optical characteristics (absorption A (λ), transmittance T (λ) and reflection R (λ)) of the films were investigated at room temperature with a computer-programmable Jasco V570 (Japan) double-beam spectrophotometer, at normal incidence in the wavelength

range of 200 to 2500 nm, with a scan speed of 400 nm/min.

3 Results and discussion

3.1 XRD analysis

Figure 1 demonstrates the XRD patterns of $(\text{PbS})_{1-x}(\text{Zn})_x$ where $x = 0, 0.01, 0.03, 0.05$ w.t%. As shown for the film of $x = 0$, all peaks correspond to PbS compounds, confirming the good purity of this film. Besides, no phases corresponding to the Zn element could be depicted for Zn-doped films, indicating that zinc was incorporated into the PbS lattice. With increasing levels of Zn-doping, both the intensity and the number of crystalline peaks decrease, indicating an increase in microstructure disorder. For pure PbS, some peaks corresponding to (111), (200), (202), (311), (222), (400), (313), (402), (422), and (511) are observed at $2\theta = 25.97, 30.084, 43.064, 50.984, 53.426, 62.535, 68.889, 70.944, 78.947$ and 84.797 respectively, which are consistent with JCPDS COD 9008694 standard data.

The favorable orientation of crystallisation in F.C.C cubic structure has occurred along the most intensive peak (200). The effect of doping leads to intensity reduction and peak broadening, which is indicated by the decrease in β -values with doping, as shown in Fig. 1 and Table 1.

The crystallite size (D), the lattice strain (ϵ), the dislocation density (δ), the lattice constant (a), d -spacing, X-ray density d_{XRD} and bulk density d_{bulk} are calculated using the following equations, respectively:

$$D = \frac{0.94\lambda}{\beta \cos \theta} \tag{1}$$

$$\epsilon = \frac{\beta \cos \theta}{4} \sim D^{-1} \tag{2}$$

$$\delta = \frac{1}{D^2} \tag{3}$$

$$a = d\sqrt{h^2 + k^2 + l^2} \tag{4}$$

Fig. 1 XRD diffraction patterns of undoped and Zn-doped PbS thin films (thickness $d = 200$ nm)

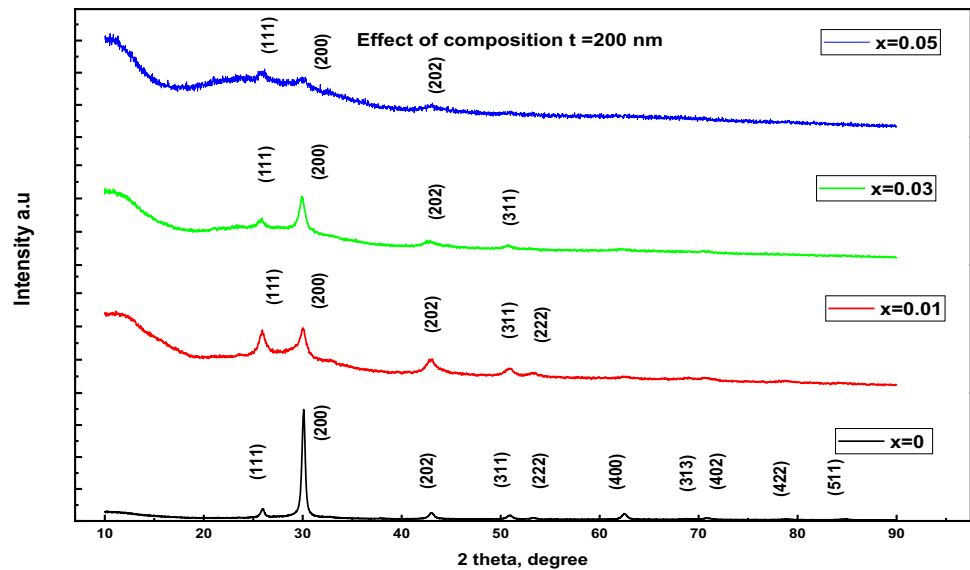


Table 1 XRD parameters of the $(\text{PbS})_{1-x}\text{Zn}_x$ films calculated using the preferred (2 0 0) orientation

X (wt%)	2θ ($^\circ$)	β ($^\circ$)	D (nm)	$\epsilon \times 10^{-3}$	$\delta \times 10^{14} \text{cm}^{-2}$	d spacing (Å)	a (Å)	V (Å^3)	d_{XRD} (gm/cm^3)	d_{bulk} (gm/cm^3)
0	30.09	0.3457	24.84	1.456	1.620	2.9663	5.9326	208.80	15.228	7.6
0.01	30.01	0.5791	14.83	2.440	4.546	2.974	5.948	210.43	15.055	7.595
0.03	29.92	0.64	13.42	2.697	5.552	2.9823	5.9646	212.2	14.673	7.586
0.05	29.88	0.64	13.40	2.699	5.561	2.9867	5.9734	213.14	14.455	7.577

$$d = \frac{\lambda}{2 \sin \theta} \quad (5)$$

$$d_{\text{XRD}} = \frac{8M_w}{N_A a^3} \quad (6)$$

$$d_{\text{bulk}} = \frac{m}{\pi r^2 h} \quad (7)$$

where θ is Bragg's angle, λ is the X-ray wavelength, Δ is the full width of the half maximum of the corresponding XRD peak, M_w is the molecular weight of $(\text{PbS})_{1-x}\text{Zn}_x$ and N_A is Avogadro's number.

As shown in Table 1, the crystallite size D decreases with Zn doping, which is characteristic of substitutional doping [34–36]. Since it is easy for doped Zn having a smaller (0.74 Å) ionic radius than that (1.19 Å) of Pb^{2+} to occupy substitutional sites in PbS lattice, leading to a reduction in the crystalline size, a matter that can be confirmed by the observed peak shift to lower θ values leading to a $\cos \theta$ increase (Eq. 1). The increase in both ε and δ with a doping level increase, which can be attributed to the defect formation in the lattice structure, could be predicted regarding Eqs. 1–3, where ε and δ are proportional to D^{-1} and D^{-2} as clear by Eqs. 2 and 3, respectively.

The microstructural parameters of grown films listed in Table 1, show that the crystallite size decreases from 24.84 to 13.40 nm when the Zn dopant concentration increases to 0.05. Besides, a rising trend in lattice defects such as micro-strain and dislocation density with increasing Zn concentration can be depicted. Such a type of change could result due to the crystalline degradation nature [37]. Furthermore, the decreases in d_{XRD} and d_{bulk} with Zn-doping could be attributed to the depicted decrease in unit cell volume [38, 39], as shown in Table 1.

The observed increases in both d -spacing and lattice constant and the cell volume $V = a^3$ may be understood regarding Eqs. 4 and 5 as the (200) peak shifting to smaller 2θ -values.

3.2 Morphological properties

Figure 2 shows SEM micro-images of $(\text{PbS})_{1-x}\text{Zn}_x$ ($x = 0, 0.01, 0.03, 0.05$ wt%) thin films deposited on glass substrates. It is revealed that the grains are homogeneously distributed on the film surface and densely agglomerated with a tendency towards

spherical shapes. The grains are different in size depending on the Zn-doping level. The average particle sizes calculated by the J-programme were found to range from 70 to 275 nm.

3.3 Elemental composition analysis (EDX)

Figure 3 shows the elemental composition analysis of the films determined by the energy-dispersive X-ray. The weight and atomic percentages of compound elements were determined. As shown, only Pb, S, and Zn elements are identified, confirming that the films are free from impurities. However, the depicted ratios of sulphur in both pure and Zn-doped PbS are smaller than their values corresponding to stoichiometric compounds. This may be attributed to the release of sulphur during the film's thermal deposition.

3.4 Linear optical characterization

Figure 4 shows the spectral variations of optical absorption $A(\lambda)$, transmission $T(\lambda)$ and reflection $R(\lambda)$ of $(\text{PbS})_{1-x}(\text{Zn})_x$ thin films, where ($x = 0, 0.01, 0.03, 0.05$ w.t%). All films reveal nearly similar spectral behaviour. They manifest relatively high absorption in the visible (~ 350 – 800 nm) range compared with their value in the NIR region, which takes almost low constant values in the NIR ($\lambda \geq 1500$ nm) range, indicating the NIR-transparent nature of the present films. Besides, with increasing the level of Zn-doping, the absorption grows less, and the fundamental edge shifts towards lower λ values, indicating an increase in the band gap energy.

Figure 4b shows that the transmission increases with λ reaching a value of 70%, confirming the good transparency of the present films in the NIR-spectral range.

As shown in Fig. 4c the present films manifest low and more intensive reflection in the VIS and NIR regions, respectively. The simultaneous decrease and increase of T and R with λ , respectively, in the NIR (~ 1200 – 2000 nm) region for all considered films suggests the occurrence of relatively high free carrier concentrations. This effect is governed by the plasma oscillation of free carriers and is associated with a shift to a shorter wavelength [39–41].

Moreover, the energy tail width of the localised states that existed in the forbidden band can be described by the following exponential Urbach

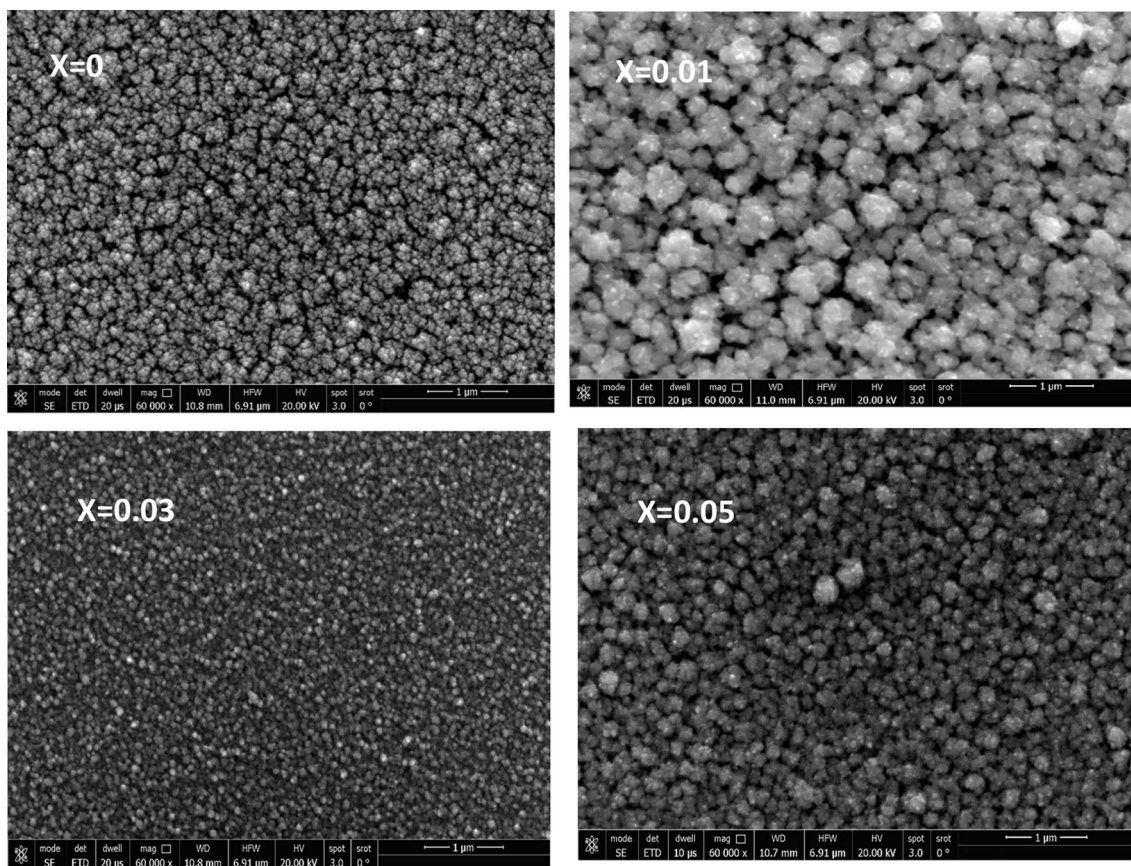


Fig. 2 SEM images of $(\text{PbS})_{1-x}\text{Zn}_x$ thin films

relation [42] in the low range of the absorption coefficient values:

$$\alpha = \alpha_0 \exp\left(\frac{h\nu}{E_u}\right), \tag{8}$$

$$\alpha = 1/d \ln\left[\frac{(1-R)^2}{T}\right] \tag{9}$$

where α_0 is a constant, E_u is the Urbach energy that measures the tail width of the localized states and d is the film thickness. The values of E_u are estimated from the slopes of $\ln(\alpha)$ Vs $h\nu$ plots as shown in Fig. 5 and recorded in Table 3. As shown E_u non-sequentially varies with Zn-doping possessing the highest value for $x = 0.03$ wt% (Table 2).

In order to determine the energy gap (E_g) values of the present films, the following Tauc’s equation [43, 44] can be utilized;

$$\alpha h\nu = \beta(h\nu - E_g)^r \text{ and} \tag{10}$$

where β is an energy-independent constant and the exponent r characterises the electronic transition type. Good fitting to straight-line portions of $(\alpha h\nu)^2$ vs $h\nu$ plots was achieved when $r = 1/2$ indicating allowed direct transitions. The value of the intercept of the linear portion with the ordinate at $(\alpha h\nu)^2 = 0$ gives the value of E_g as shown in Fig. 6. The determined values of E_g are recorded in Table 3. It is clear that E_g increases from 1.25 to 1.64 with increasing Zn-doping level which is consistent with other reported results [45].

The surface SELF and volume VELF energy losses functions utilised to certify the electromagnetic radiation dealing with the material surface and bulk and the interaction with the material electrons are given by the following relations [46, 47], respectively.

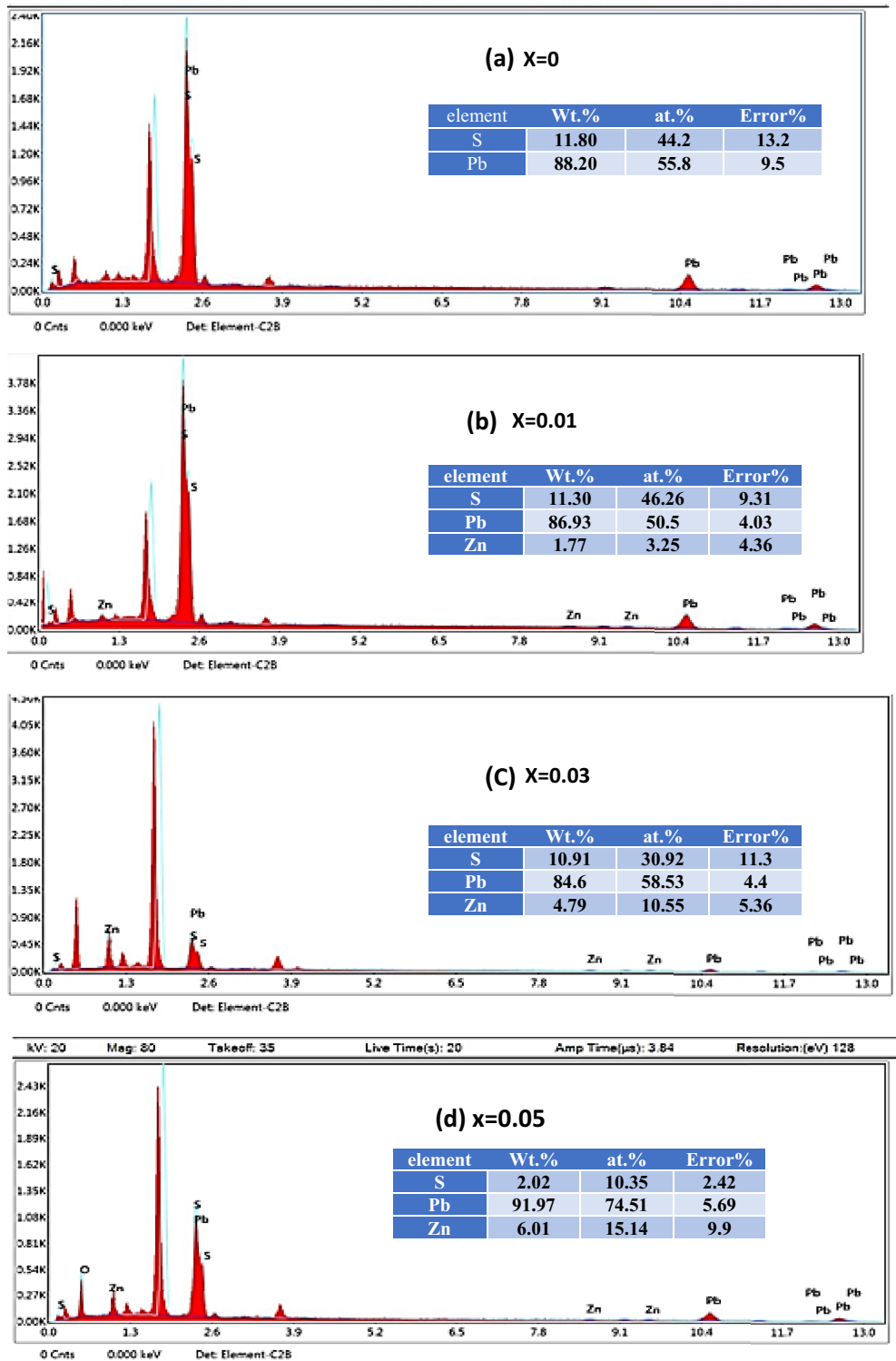


Fig. 3 EDX for $(\text{PbS})_{1-x}\text{Zn}_x$ films at $x=0$ (a), $x=0.01$ (b), $x=0.03$ (c) and $x=0.05$ (d)

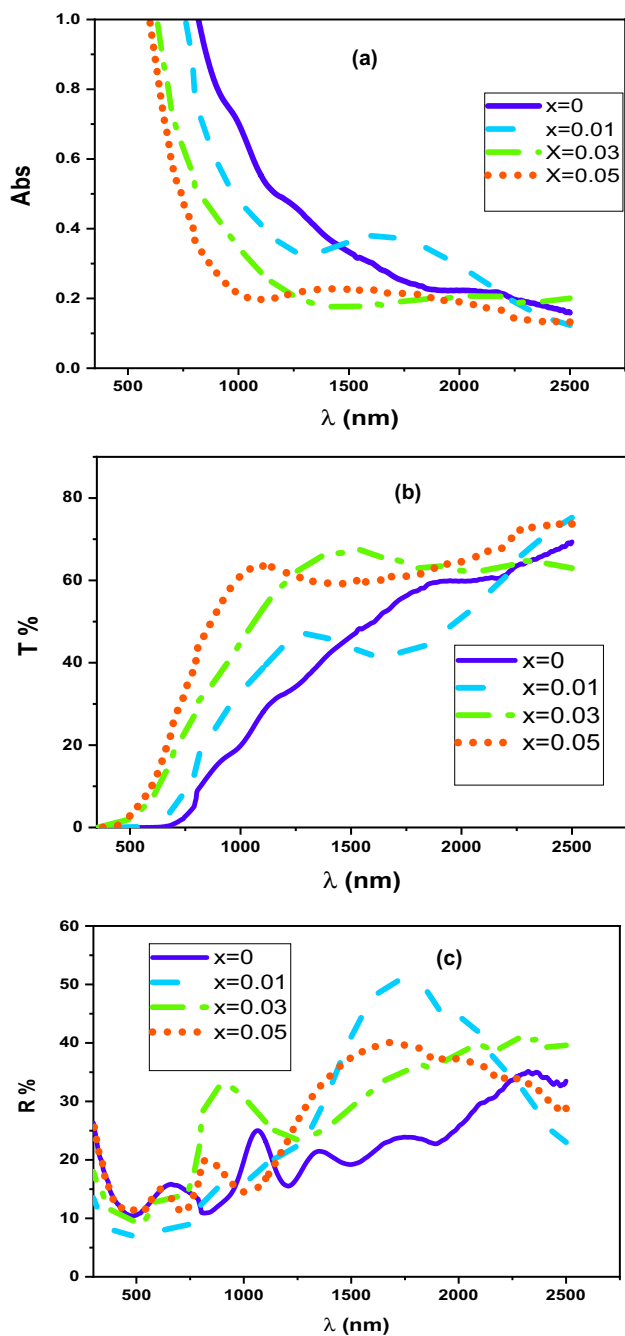


Fig. 4 a Optical absorption, b transmission, and c Reflection spectra of $(\text{PbS})_{1-x}\text{Zn}_x$ thin films where $d=200$ nm

$$\text{SELF} = \frac{\epsilon_{im}}{(\epsilon_r^2 + 1)^2 + \epsilon_{im}^2} \tag{11}$$

$$\text{VELF} = \frac{\epsilon_{im}}{\epsilon_r^2 + \epsilon_{im}^2} \tag{12}$$

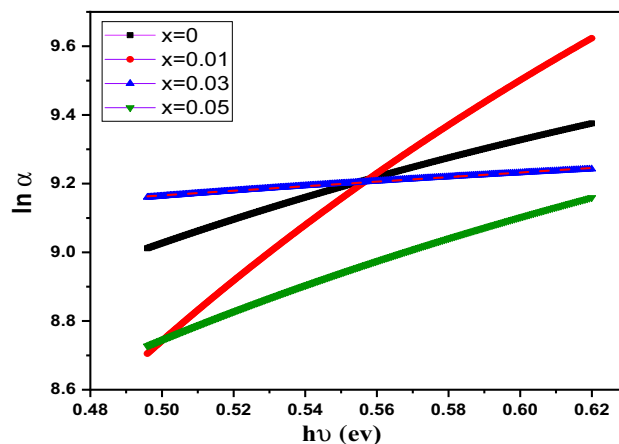


Fig. 5 Plots of $(\ln \alpha - h\nu)$ for $(\text{PbS})_{1-x}\text{Zn}_x$ thin films

Table 2 Values of absorption coefficient measured at a solar maximum wavelength ($\lambda=500$ nm), as well as, values of, the energy band gap E_g , and Urbach energy E_u for $(\text{PbS})_{1-x}\text{Zn}_x$ compounds

X (wt%)	$\alpha_{500} \times (10^5 \text{ cm}^{-1})$	E_g (ev)	E_u (ev)
0	2.5	1.25	0.34
0.01	1.88	1.43	0.13
0.03	0.69	1.55	1.50
0.05	0.63	1.64	0.29

where ϵ_r and ϵ_{im} are the real and imaginary dielectric constant components, respectively. As shown in Fig. 7, the energy dependence of SELF and VELF functions for films of $x=0.03$ at $d=150$ nm and 200 nm have almost the same behaviour, where each of them manifests two essential lower and higher peak intensities. However, the intensities of the VELF peaks are more intense than their corresponding SELF peaks by 4.95, 8.28 and 2.125, 4.9 times for the I and II peaks of the films of 150 and 200 nm, respectively. This may be attributed to the relatively larger penetration depth of electromagnetic radiation and interactions with more involved electrons.

The studies of optical dielectric and dispersion and the determination of their parameters are important due to their roles in optical communication development and optical device performance [48]. As shown in Fig. 8, the plots of the real dielectric constant versus λ^2 are linear in the λ (2300–2470 nm) range, realising the following Spitzer-Fan equation [49–51],

Table 3 Values of dielectric and dispersion parameters for (PbS)_{1-x}Zn_x compounds

X (wt%)	N (10 ²⁰ cm ⁻³)	ε _L	E _d (ev)	E _o (ev)	n _o	ε _∞	X _c	ω _p (10 ¹⁴ s ⁻¹)
0	1.71	29.24	4.197	0.697	2.65	7.02	2.33	7.39
0.01	1.61	39.30	1.017	0.578	1.66	2.76	3.13	7.15
0.03	1.28	38.05	6.26	0.71	3.13	9.79	3.03	6.39
0.05	1.22	34.58	2.13	0.620	2.11	4.45	2.75	6.24

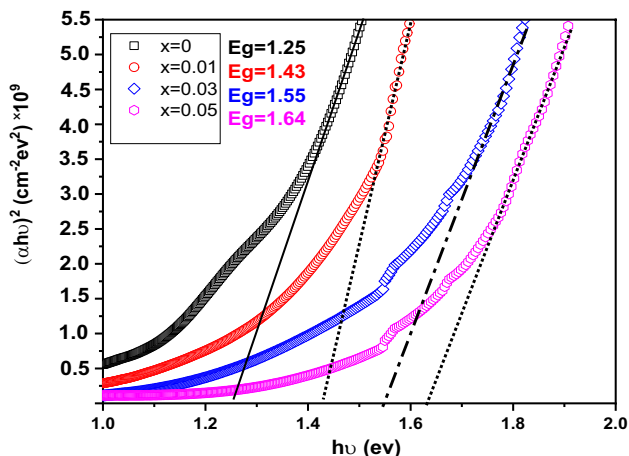


Fig. 6 Plots of $(ahv)^2$ vs. hv for (PbS)_{1-x}Zn_x thin films

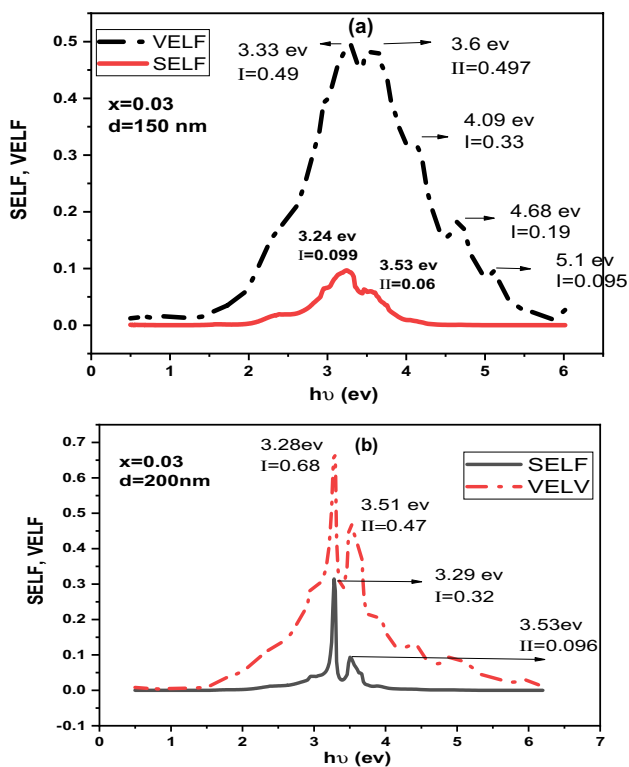


Fig. 7 Energy dependences of volume (VELF) and surface (SELF) of (PbS)_{0.97}Zn_{0.03} thin films 150 nm (a) and 200 nm (b) thick

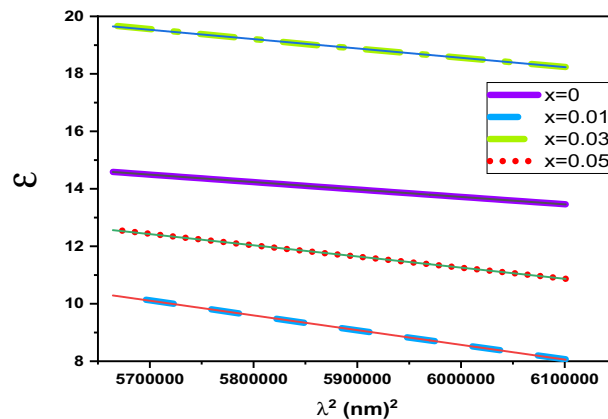


Fig. 8 Plots of $(\epsilon - \lambda^2)$ for (PbS)_{1-x}Zn_x thin films

$$\epsilon' = \epsilon_L - \left(\frac{e^2}{\pi c^2} \right) \frac{N}{m^*} \lambda^2 \tag{13}$$

$$= \epsilon_L + 4\pi\chi_c \tag{14}$$

$$= \epsilon_L - \left(\frac{\lambda}{\lambda_p} \right)^2 \tag{15}$$

where ϵ_L is the high-frequency dielectric constant of the lattice, N/m^* is the free carrier concentration to the effective mass, χ_c is the free carrier's contribution in the real part of the dielectric constant and λ_p is plasma wavelength. These parameters were determined using the plot's slopes and intercepts and recorded in Table 3.

In the same λ -range of normal dispersion $\sim 2300\text{--}2470 \text{ nm}$ ($n^2 - 1$)⁻¹ vs $(hv)^2$ plots are linearly verifying the Wemple–Didomenico single oscillator model [35], expressed by the following relation;

$$(n^2 - 1)^{-1} = \frac{E_o^2 - (hv)^2}{E_o E_d} \tag{16}$$

where E_o and E_d are the oscillator and the dispersion parameters, respectively. E_o and E_d can be calculated

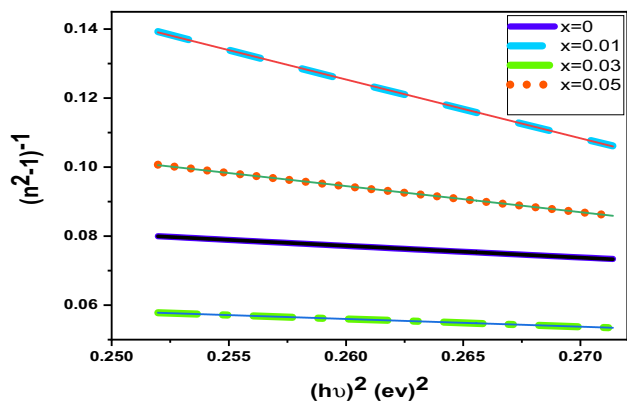


Fig. 9 $(n^2 - 1)^{-1}$ vs. $(hv)^2$ plots for $(PbS)_{1-x}Zn_x$ thin films

with the help of the slopes and intercepts of the plots in Fig. 9 and recorded in Table 3.

3.5 Non-linear optical characterization

The optical linear and non-linear effects are subjected to the induced optical power level and the material optical response. At low optical power, the bound electron of an atom is affected by a harmonic electrical restoring force that leads to small symmetrical harmonic displacements of the electron around its original position. The values of these displacements are linearly dependent on the electric force, and optical properties like polarisation depend linearly on the electric fields. Such optical linear effects take place only at power levels lower than the binding electric field intensity of the bound electrons. However, the optical non-linearity is due to the anharmonic response of the medium induced by intensive electric fields, such as the very powerful laser field. This leads to asymmetric polarisation that is no longer linearly proportional to the electric field [52].

Thus, the polarisation (P) in a medium could be resulted from linear and non-linear susceptibility contributions, depending on the applied light power intensity, i.e.

$$P = \chi^1 E + P_{NL}; P_{NL} = \chi^{(2)} E^{(2)} + \chi^{(3)} E^{(3)} \tag{17}$$

where χ^1 is the linear susceptibility, P_{NL} is the non-linear optical polarizability, and $\chi^{(2)}$ and $\chi^{(3)}$ are the 2nd and 3rd order of the non-linear optical susceptibilities, respectively.

The linear susceptibility can be determined using the following equation[53]

$$\chi^{(1)} = \frac{n_0^2 - 1}{4\pi} \tag{18}$$

where $n_0 = \sqrt{\frac{E_d}{E_0} + 1}$ is the static refractive index given by the value of n when $h\nu = 0$ in Eq. (16)

Miller’s generalized rule [54] has correlated $\chi^{(3)}$ to $\chi^{(1)}$ through the following expression,

$$\chi^{(3)} = A(\chi^{(1)})^4 = \frac{A}{(4\pi)^4} (n_0^2 - 1)^4 \tag{19}$$

where $A = 1.7 \times 10^{-10}$ esu which is valid almost for all materials [55].

The non-linear refractive index n_2 is related to $\chi^{(3)}$, according to Tichy and Ticha [53], as follows;

$$n_2 = \frac{12\pi\chi^{(3)}}{n_0} \tag{20}$$

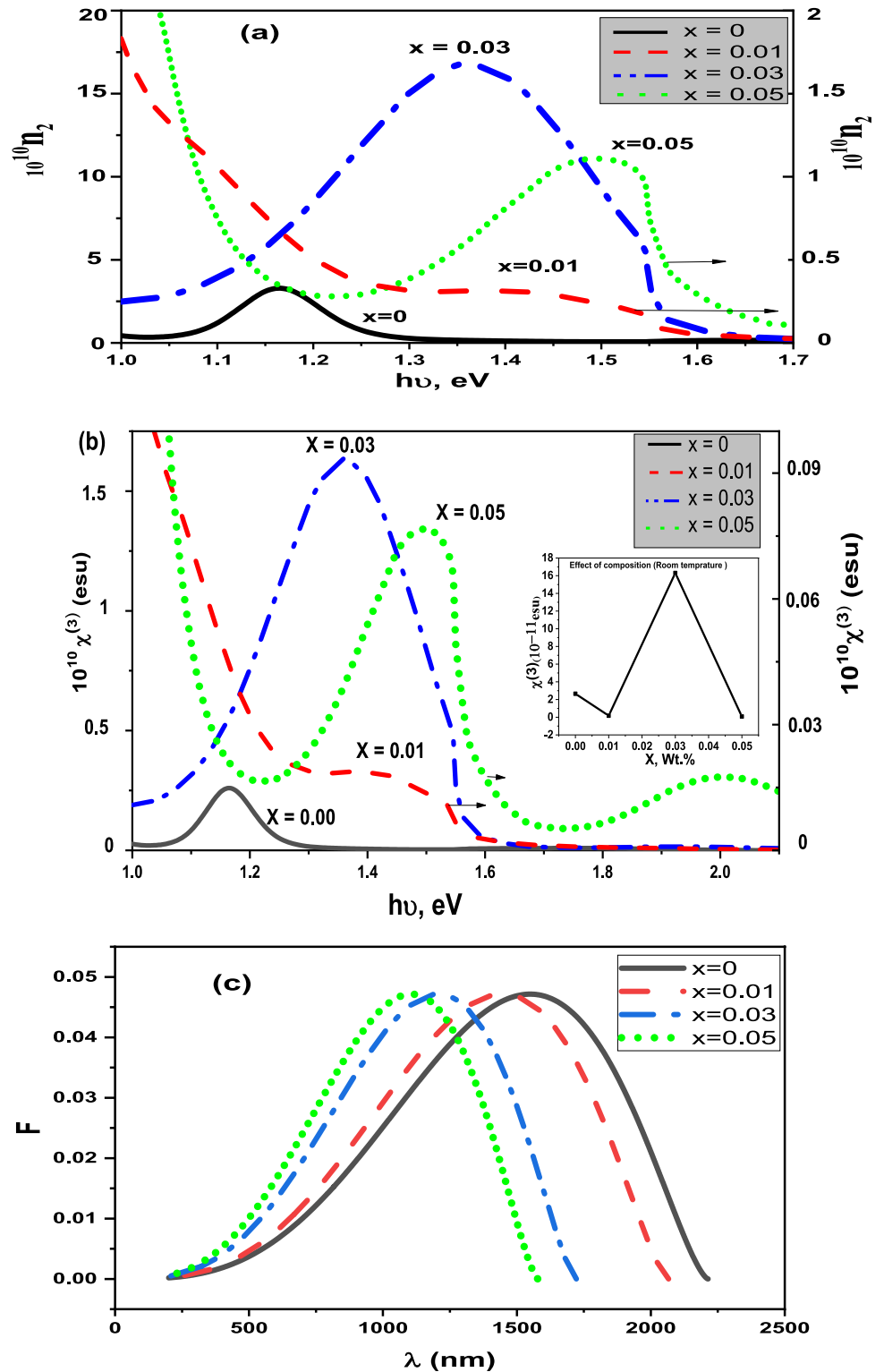
Both the non-linear refractive index n_2 and third-order optical polarizability $\chi^{(3)}$ are crucial parameters for numerous optical non-linear applications [56–59]. $\chi^{(3)}$ describes third harmonic generation, two-photon absorption, and intensity-dependent refractive index, and plays an important role in the specification of material validity for non-linear optical systems. Besides, n_2 is an essential parameter for the performance of nonlinear optical devices [60]. Furthermore, the energy dispersion of the nonlinear absorption coefficient is described by the so-called F-function [61, 62]; where

$$F = \left[\left(\frac{2h\nu}{E_g} \right) - 1 \right]^{3/2} / \left(\frac{2h\nu}{E_g} \right)^5 \tag{21}$$

This F -function, which depends on the energy band structure, is important to specify the energy states that are coupled. Variations of the energy dependences of n_2 , $\chi^{(3)}$ and F -function influenced by Zn-doping, film thickness, and annealing temperature are given in Figs. 10, 11, and 12, respectively. The maximum values of these non-linear parameters were estimated and recorded in Table 4.

As shown in Fig. 10a, b, n_2 and $\chi^{(3)}$ have the same spectral variation. Depending on the film band gap energy, they start to increase with increasing the photon energy to a maximum value, then decrease with further energy increases and start tending to a constant value. Besides n_2 and $\chi^{(3)}$ maxima of the same films lie approximately at the same energy value,

Fig. 10 Spectral variations of n_2 , $\chi^{(3)}$ and F- function for $(\text{PbS})_{1-x}\text{Zn}_x$ films. ($x=0, 0.01, 0.03$ and 0.05 Wt.%) $d=200$ nm



which is generally shifted towards the higher values as Zn-doping levels increase. As shown in Fig. 10b and Table 4, the moderate (2.65×10^{-11} esu) value of $\chi_{\text{max}}^{(3)}$

of pure PbS may be partially attributed to one or more of the different contributing factors. Chalcogenides containing, in general, highly polarizable atoms and/

Fig. 11 n_2 (a), $\chi^{(3)}$ (b) of $(\text{PbS})_{1-x}\text{Zn}_x$, $x=0.03$ W.t% thin films at different thicknesses

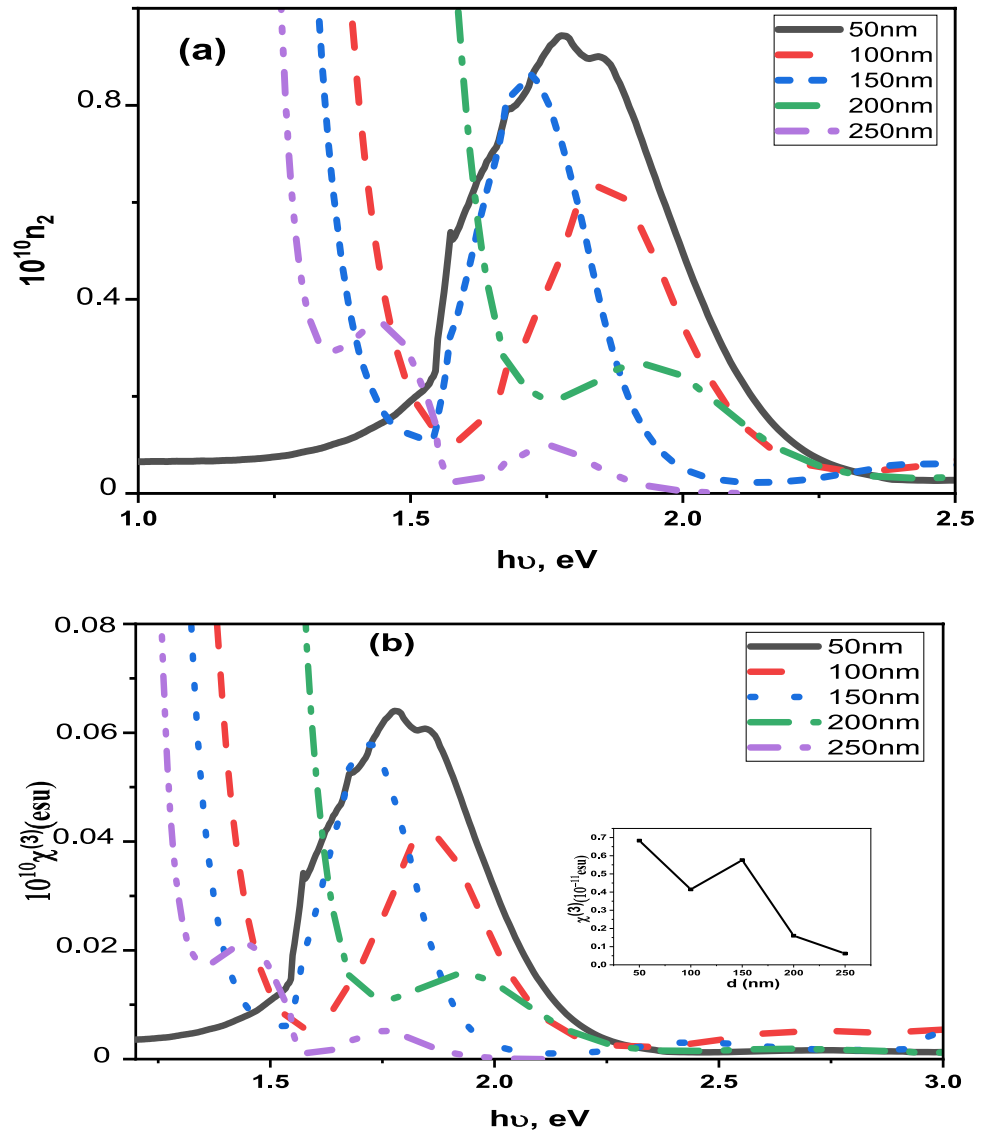


Fig. 12 Effect of annealing on $\chi^{(3)}$ ($x=0.03$, $d=50$ nm)

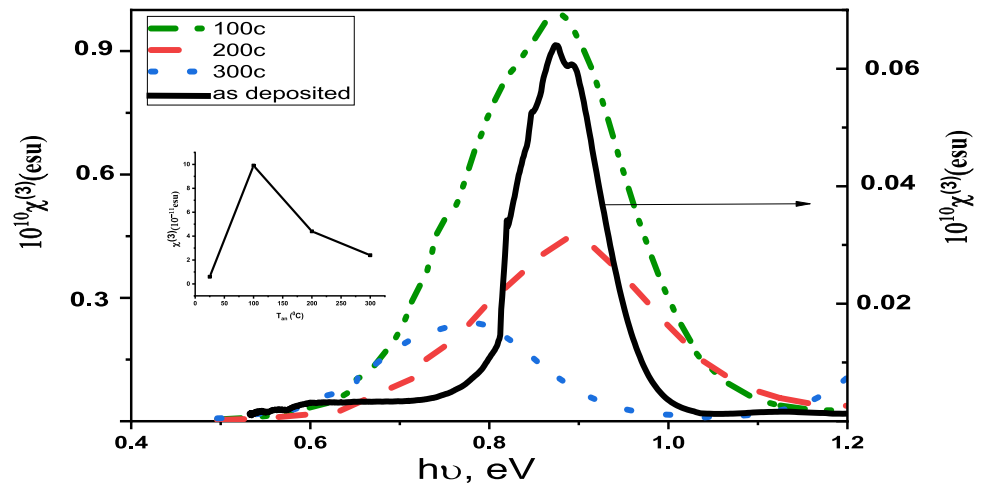


Table 4 Effect of film composition on Non-linear parameters for $(\text{PbS})_{1-x}\text{Zn}_x$ films, $d=200$ nm

Materials	$10^{13} n_2$	$10^{13} \chi^{(3)}(\text{esu})$	References
0	3320	265	Present work
0.01	3070	17.30	
0.03	16,800	16,300	
0.05	11,800	7.60	
PbS	741,700	74,280	[59]
CdO	0.38	0.0135	[64]
Zn doped CdO	1.32	0.0573	[64]
$\text{As}_{40}\text{S}_{45}\text{Se}_{15}$	32.4	19.40	[67]
Thieno[2,3-b]thiophene	1238	2.50	[30]
$\text{Ge}_{20}\text{Se}_{75}\text{In}_5$	0.0000102	156	[68]
MnO_2	0.00508	0.636	[65]
CuO	0.00535	0.670	[65]

or ions in the material matrix are expected to have large non-linear properties. Lead Pb^{82} has a relatively large number of cloud electrons in the outer shell, which are placed far apart from the nucleus. This simplifies the polarisation process. Besides, the relatively long length of 0.29696 nm of the Pb–S bond [31, 32] strongly contributes to the polarisation in the optical medium. Finally, the relatively higher value of grain size (Table 1) of pure PbS film means higher values of material compactness, and consequently, the refractive index increases, indicating a high number of polarizable Pb–S bonds (Fig. 13).

Besides, the observed decrease of $\chi^{(3)}$ with inserting Zn-dopant with $x = 0.01$ wt% may be due to the

formation of Zn–S bonds with a lower bond length (0.27805 nm) on the expense of Pb–S with a larger bond length (0.29696 nm) [31, 32]. With increasing Zn-doping up to $x = 0.03$ the value of $\chi^{(3)}$ remarkably increases to be 1.63×10^{-10} esu, which may be attributed to the increase in defect formation in the material structure [31, 33] in addition to the energy activated of both Pb–S and Zn–S bonds. The rapid decline of $\chi^{(3)}$ with a further increase of Zn-doping level up to $x = 0.05$ wt% could be interpreted by the extra formation of weak polarizable (Zn–S bonds) instead of the relatively stronger (Pb–S) ones, and/or the decrease of the densities of both Pb–S and Zn–S bonds as a result of the depicted relatively higher deficiency of sulphur content in this film.

Figure 10c depicts the spectral variations of F-function for pure and Zn-doped films. F-function begins increasing at energy values of 0.57, 0.61, 0.73, and $0.78 > E_g/2$ eV for films with $x = 0, 0.01, 0.03,$ and 0.05 Wt.%, attaining its maximum values at 0.80, 0.86, 1.03 and 1.12 eV then it decreases with further $h\nu$ -increase inclining to a constant value at 1.04, 1.11, 1.33 and 1.46 eV $< E_g$. This behaviour of $F - h\nu$ satisfies the two-photon absorption condition $E_g/2 < h\nu < E_g$. Besides, the ratio of $E_g/F_{E_{\text{max}}}$ of the energy gap and the energy position of $F_{E_{\text{max}}}$ were found 1.56, 1.66, 1.50 and 1.45 for $x = 0, 0.01, 0.03$ and 0.05 Wt.% of the present $(\text{PbS})_{1-x}\text{Zn}_x$ thin films. These ratio values are close to the reported values of 1.4 for different chalcogenide materials [63–66], realising the condition of two-photon absorption.

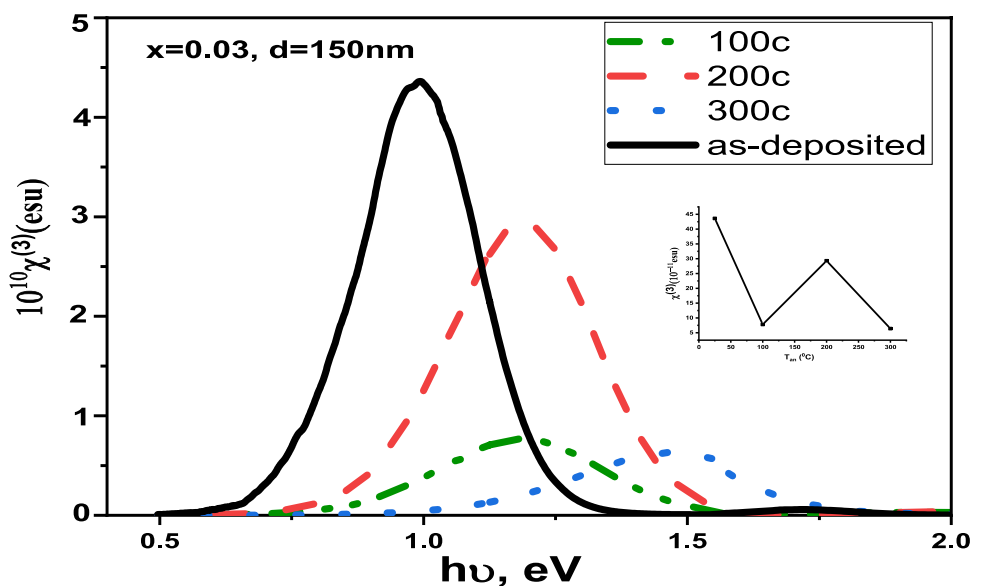
Fig. 13 Effect of annealing on $\chi^{(3)}$ values for $(\text{PbS})_{0.97}\text{Zn}_{0.03}$ ($d = 150$ nm)

Table 5 Effect of film thickness and annealing temperature on Non-linear parameters, $x = 0.03$ Wt.%

d (nm)/room temperature		α_{500}	E_g (ev)	$10^{10} n_2$	$10^{11} \chi^{(3)}$ (esu)
Room	50	75,382	1.66	9.42	0.683
tempera- ture	100	46,247	1.60	6.31	0.415
	150	29,694	1.58	8.59	0.576
	200	46,910	1.55	2.65	0.16
	250	44,923	1.20	0.94	0.062
T_{an} (°C)/ d (nm)					
100	50 nm	15,684	2.3	10.79	9.9
		14,044	2.42	5.3	4.4
		5100	2.69	3.04	2.4
200	150 nm	1050	1.63	8.6	7.8
		1050	1.68	27.8	29.3
		843	1.93	7.3	6.4

In a trial to enhance the best values 16.8×10^{-10} and 1.63×10^{-10} esu attained for $n_2, \chi^{(3)}$, respectively, by the film of $x = 0.03$ at $d = 200$ nm, the effects of both film thickness and annealing temperature were examined. To avoid repetition, the optical parameters affected by either the film thickness or annealing temperature and required for NLO-calculations were determined by the same method employed here.

As shown in Figs. 11, 12 and Table 4, both $n_2, \chi^{(3)}$ values are generally decreased with film thickness increase. This may be mainly attributed to the increase of the weak polarizable Zn-S bonds on the expense of the strong Pb-S ones.

Besides, the decrease in material density and consequently the decrease of the refractive index, the thermally eliminated localized states as well as the density decrease of both Zn-S and Pb-S polarizable bonds as a result of sulfur release may be responsible for the relatively low values of both $n_2, \chi^{(3)}$ with annealing. Nevertheless the enhancing and inhibiting factors of non-linear properties which were previously discussed could be comprmized leading to attain the enhanced $2.78 \times 10^{-10}, 2.93 \times 10^{-10}$ esu result of n_2 and $\chi^{(3)}$ for annealed (at 200 °C) films of 150 nm thick. As shown in Tables 4 and 5 these results are comparable with the reported ones of some oxides, chalcogenide and organic materials.

4 Summary and conclusions

The $(PbS)_{1-x}(Zn)_x$ thin films with light Zn-doping were deposited using the thermal deposition technique, analysed by XRD, SEM and EDS and characterised by UV-VIS-NIR spectroscopy. PbS films crystallise in F.C.C structure with a preferable (200) orientation. The grains on the film surfaces are homogeneously distributed, with an average particle size 34–64 nm depending on the Zn-dopant ratio. With the increase in Zn-doping concentration, the grain size decreases while the microstructure disorder, microstrain, and dislocation density increase.

The lower sulphur ratios revealed for either Zn-doped or undoped films than their corresponding stoichiometric values are dependent on the thermal deposition conditions.

The films show an allowed direct transition with an energy gap value that increases with Zn-doping and annealing temperature, but decreases with increasing film thickness.

Absorption, dielectric, and dispersion parameters varied depending on Zn-doping, film thickness, and annealing temperature, which strongly affect the optical NLO properties.

Finally, the satisfactorily enhanced 2.78×10^{-10} and 2.93×10^{-10} esu values of n_2 and $\chi^{(3)}$, respectively, obtained for $(PbS)_{0.97}(Zn)_{0.03}$ films of 150 nm thick and annealed at 200 °C may recommend such films be applied in highly intensive optical radiation systems.

Funding

Open access funding provided by The Science, Technology & Innovation Funding Authority (STDF) in cooperation with The Egyptian Knowledge Bank (EKB).

Open Access This article is licensed under a Creative Commons Attribution 4.0 International License, which permits use, sharing, adaptation, distribution and reproduction in any medium or format, as long as you give appropriate credit to the original author(s) and the source, provide a link to the Creative Commons licence, and indicate if changes were made. The images or other third party material in this article are included in the article’s Creative Commons licence, unless indicated otherwise in a credit line to the material. If material is not included in the article’s

Creative Commons licence and your intended use is not permitted by statutory regulation or exceeds the permitted use, you will need to obtain permission directly from the copyright holder. To view a copy of this licence, visit <http://creativecommons.org/licenses/by/4.0/>.

References

- J. Vigneron, A. Redon, R. Heindl, J.-C. Martin, C. Sella, *Solar Cells* **5**, 25 (1981)
- L.D. Madsen, L. Weaver, *J. Am. Ceram. Soc.* **81**, 988 (1998)
- S. Chao, Y.-F. Huang, Y.C. Chen, L. Yan, *J. Phys. D* **23**, 955 (1990)
- P. Gao, Y. Liu, W. Lv et al., *J. Power. Sources* **265**, 192 (2014)
- L.M. Droessler, *Lead oxides for photovoltaics* (2014)
- S. Darbe, R. Beal, A. Stavrinadis, et al., *Summer Stud. Rep.* (2009)
- S.I. Sadovnikov, A.I. Gusev, A.A. Rempel, *Russ. Chem. Rev.* **85**, 731 (2016)
- Z. Fan, L.-C. Lin, W. Buijs, T.J. Vlugt, M.A. Van Huis, *Nat. Commun.* **7**, 11503 (2016)
- J. Patel, F. Mighri, A. Ajji, D. Tiwari, T.K. Chaudhuri, *Appl. Phys. A* **117**, 1791 (2014)
- Z. Sun, Z. Liu, J. Li, S.P. Ga Tai, F.Y. Lau, *Adv. Mater.* **24**, 5878 (2012)
- K.-I. Hanaki, A. Momo, T. Oku et al., *Biochem. Biophys. Res. Commun.* **302**, 496 (2003)
- M.O. Aboelez, M.S. Kamel, A. Belal et al., *Mol. Divers.* **27**, 901 (2023)
- J.M. Skelton, S.C. Parker, A. Togo, I. Tanaka, A. Walsh, *Phys. Rev. B* **89**, 205203 (2014)
- M. Li, X. Wang, H. Ruan et al., *J. Alloys Compd.* **768**, 399 (2018)
- J. Tang, L. Brzozowski, D.A.R. Barkhouse et al., *ACS Nano* **4**, 869 (2010)
- J.M. Luther, J. Gao, M.T. Lloyd, O.E. Semonin, M.C. Beard, A.J. Nozik, *Adv. Mater.* **22**, 3704 (2010)
- C.-H.M. Chuang, P.R. Brown, V. Bulović, M.G. Bawendi, *Nat. Mater.* **13**, 796 (2014)
- K.P. Bhandari, P.J. Roland, H. Mahabaduge et al., *Sol. Energy Mater. Sol. Cells* **117**, 476 (2013)
- B. Ding, T. Gao, Y. Wang, D.H. Waldeck, P.W. Leu, J.-K. Lee, *Sol. Energy Mater. Sol. Cells* **128**, 386 (2014)
- S. Seghaier, N. Kamoun, R. Brini, A. Amara, *Mater. Chem. Phys.* **97**, 71 (2006)
- E.K. Shokr, H.A. Mohamed, H. Mohamed, M.S. Kamel, H. Ali, *Phys. Scr.* **98**, 085917 (2023)
- F.W. Wise, *Acc. Chem. Res.* **33**, 773 (2000)
- S. Thangavel, S. Ganesan, S. Chandramohan, P. Sudhagar, Y.S. Kang, C.-H. Hong, *J. Alloys Compd.* **495**, 234 (2010)
- R. Bai, D. Kumar, S. Chaudhary, D.K. Pandya, *Acta Mater.* **131**, 11 (2017)
- E. Pentia, L. Pintilie, I. Matei, T. Botila, E. Ozbay, *J. Optoelectron. Adv. Mater.* **3**, 525 (2001)
- S. Kumar, T. Sharma, M. Zulfequar, M. Husain, *Physica B* **325**, 8 (2003)
- B. Thangaraju, P. Kaliannan, *Semicond. Sci. Technol.* **15**, 849 (2000)
- B. Touati, A. Gassoumi, S. Alfaify, N. Kamoun-Turki, *Mater. Sci. Semicond. Process.* **34**, 82 (2015)
- I. Sharma, S. Tripathi, P. Barman, *Phase Transit.* **87**, 363 (2014)
- E.K. Shokr, M.S. Kamel, H. Abdel-Ghany, M.A.E.A.A. Ali, A. Abdou, *Mater. Chem. Phys.* **290**, 126646 (2022)
- M. Liu, W. Li, Y. Wang, Q. He, *Physica B* **545**, 245 (2018)
- R.K. Joshi, A. Kanjilal, H. Sehgal, *Nanotechnology* **14**, 809 (2003)
- A. Gassoumi, S. Alleg, N. Kamoun-Turki, *J. Mol. Struct.* **1116**, 67 (2016)
- N. Neto, Y. Oliveira, C. Paskocimas, M. Bomio, F. Motta, *J. Mater. Sci.* **29**, 19052 (2018)
- A. Nakrela, N. Benramdane, A. Bouzidi, Z. Kebbab, M. Medles, C. Mathieu, *Results Phys.* **6**, 133 (2016)
- N.F.A. de Neto, O.B. de Medeiros Ramalho, H. Fantucci, R.M. dos Santos, M. Bomio, F.V. da Motta, *J. Mater. Sci.* **31**, 14192 (2020)
- E. Sarica, V. Bilgin, *Mater. Sci. Semicond. Process.* **68**, 288 (2017)
- W. Mohamed, N. Hadia, M. Alzaid, A.M. Abu-Dief, *Solid State Sci.* **125**, 106841 (2022)
- E. Shanthi, V. Dutta, A. Banerjee, K. Chopra, *J. Appl. Phys.* **51**, 6243 (1980)
- K. Chopra, S. Major, D. Pandya, *Thin Solid Films* **102**, 1 (1983)
- E.K. Shokr, *Semicond. Sci. Technol.* **15**, 247 (2000)
- F. Urbach, *Phys. Rev.* **92**, 1324 (1953)
- N.F. Mott, E.A. Davis, *Electronic Processes in Non-crystalline Materials* (Oxford University Press, Oxford, 2012)
- J. Singh, K. Shimakawa, *Advances in Amorphous Semiconductors, advanced in condensed matter science*, vol. 5 (2003)
- A. Ekinici, Ö. Şahin, S. Horoz, *J. Mater. Sci.* **31**, 1210 (2020)
- J.I. Pankove, *Optical Processes in Semiconductors* (Courier Corporation, North Chelmsford, 1975)

47. H. Zeyada, M. Youssif, N. El-Ghamaz, M. Aboderbala, *Physica B* **506**, 75 (2017)
48. A. Farag, I. Yahia, *Opt. Commun.* **283**, 4310 (2010)
49. F. Yakuphanoglu, M. Sekerci, O. Ozturk, *Opt. Commun.* **239**, 275 (2004)
50. H. Afify, A.-S. Gadallah, M. El-Nahass, M.A. Khedr, *J. Mol. Struct.* **1098**, 161 (2015)
51. W. Steinmann, *Physica Status Solidi (b)* **28**, 437 (1968)
52. P. Sharma, S. Katyal, *J. Appl. Phys.* **107**, 11 (2010)
53. H. Ticha, L. Tichy, *J. Optoelectron. Adv. Mater.* **4**, 381 (2002)
54. C.C. Wang, *Phys. Rev. B* **2**, 2045 (1970)
55. M. El-Nahass, H.A. El-Khalek, A.M. Nawar, *Eur. Phys. J. Appl. Phys.* **57**, 30201 (2012)
56. E.A. Romanova, Y.S. Kuzyutkina, V.S. Shiryaev, S. Guizard, *Quantum Electron.* **48**, 228 (2018)
57. M. Diouf, A.B. Salem, R. Cherif, A. Wague, M. Zghal, *Opt. Mater.* **55**, 10 (2016)
58. M. Diouf, A.B. Salem, R. Cherif, H. Saghaei, A. Wague, *Appl. Opt.* **56**, 163 (2017)
59. K.V. Chandekar, F.H. Alkallas, A.B.G. Trabelsi et al., *Physica B* **641**, 414099 (2022)
60. H. Zeyada, M. Makhlof, *Opt. Mater.* **54**, 181 (2016)
61. J. Stevels, *Proceedings 11th International Congress Pure and Applied Chemistry*, vol. 5 (1975), pp. 519–523
62. L. Petit, N. Carlie, R. Villeneuve et al., *J. Non-Cryst. Solids* **352**, 5413 (2006)
63. H. Abdelmaksoud, F. A. Abdel-Wahab, *The Impact of Dysprosium Ions as a Dopant on Linear and Nonlinear Optical Dispersion Parameters in a-Se Thin Film*, (Scientific & Academic Publishing) vol. 8 (2018), pp. 1–8.
64. I. Yahia, G. Salem, J. Iqbal, F. Yakuphanoglu, *Physica B* **511**, 54 (2017)
65. S. Mansour, M. Hassaan, A. Emara, *Phys. Scr.* **89**, 115812 (2014)
66. J. Requejo-Isidro, A. Mairaj, V. Pruneri, D. Hewak, M. Netti, J. Baumberg, *J. Non-Cryst. Solids* **317**, 241 (2003)
67. E.R. Shaaban, M.Y. Hassaan, M. Moustafa, A. Qasem, G.A. Ali, *Optik* **186**, 275 (2019)
68. I. Sharma, S. Tripathi, P. Barman, *Phase Transit.* **363**, 375 (2014)

Publisher's Note Springer Nature remains neutral with regard to jurisdictional claims in published maps and institutional affiliations.